Focusing of a relativistic electron beam with a microfabricated quadrupole magnet

Benjamin A. Pound and Robert Candler

Department of Electrical and Computer Engineering, University of California,
Los Angeles, California 90095, USA

Sophie Crisp, Alexander Ody, Pietro Musumeci, and James Rosenzweig

Department of Physics, University of California, Los Angeles, California 90095, USA

The application of microfabrication techniques to beam physics responds to a need in the particle accelerator community for miniature, economical components that can be used in a range of diverse applications. In this work, we show the first reported results of relativistic (3.2 MeV kinetic energy) electron beam focusing using a microfabricated Panofsky-like quadrupole. The measurements revealed a spurious vertical steering dipole field which was corrected by asymmetrically exciting the currents in the device. The differences between experimental data and expected results are investigated with the help of RADIA simulations.

I. INTRODUCTION

Relativistic electron beams are used in a variety of applications, such as x-ray generation [1–5], cancer therapy [6], cargo inspection [7], nanofabrication [8], polymer curing [9], and more. All relativistic electron accelerators incorporate magnetic elements to steer, focus, and correct aberrations in the beam. The current emphasis on smaller and cheaper accelerator systems requires a corresponding effort to develop more compact magnet beam optics. To this end, we present in this work a microfabricated Panofsky-like quadrupole (MPQ) as shown in Fig. 1, characterized through theory, simulation, and experiment. The benefits of such a device over other microfabricated quadrupole designs are a simpler fabrication process, arbitrary length (from submillimeter to 100s millimeters), and the ability to operate with an adjustable gap. The device can provide uniform magnetic gradients greater than 100 T/m.

Quadrupoles are characterized by both their transverse gradient B' and effective magnetic length L_m, which is the transverse magnetic gradient integrated along the beam axis through the quadrupole magnet, divided by the peak gradient. A thin quadrupole works as a "lens" for charged particles with focal length $f = \pm \frac{p}{q} \frac{1}{B' L_m}$, where q is the electron charge and p is the particle momentum.

There are several quadrupole devices in the literature that leverage microfabrication techniques. Microfabrication is appealing because (i) the high thermal conductivity and capacity of silicon allow high current density ($\sim 1 \times 10^{10}$ A/m^2) in thin copper traces [10], (ii) hundreds or thousands of identical components can be made in parallel on a single substrate, and (iii) feature size and alignment between individual devices (such as a quadrupole multiplet) is automatically satisfied with single micron precision or better across the entire substrate [11].

Microfabricated devices based on static electric fields have been used in miniature mass spectrometers [12]. Focusing devices based on electromagnetic waves have been employed to control the transverse size in dielectric laser accelerators [13]. In that work, a photonic crystal based lens driven by a 2-μm laser was shown to be equivalent to quadrupole gradients in the MT/m range, but these structures have an extremely small gap (on the order of the optical scale) and are severely limited in the amount of transmitted current. Finally, our group previously reported a microfabricated conventional magnetic quadrupole [14] with potential for gradients of $\sim$100–1000 T/m, but the magnetic length is limited to less than 1 mm due to the limits of thick film, high aspect ratio electroplating. The closest relative to the devices discussed in this paper are quadrupoles fabricated directly as a printed circuit board (PCB) [15,16] which leverage processing techniques similar to microfabrication but suffer from inferior PCB thermal characteristics and less precise intrasubstrate alignment.

The gradient for conventional electromagnet quadrupoles with soft iron pole tips can be estimated as $B' = \frac{2\mu_0 NI}{r^2}$,
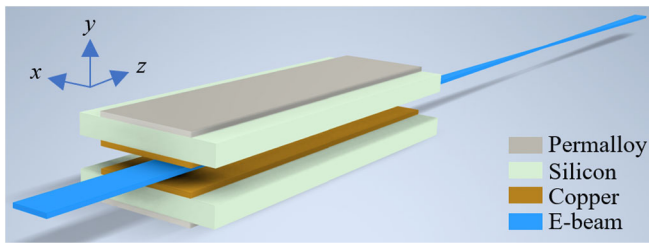
FIG. 1. Model of the MPQ (with the indicated structure and materials) focusing an electron beam. To focus this electron beam, the current in both copper sheets is directed in the $-z$ direction. We use the indicated coordinate system throughout this manuscript.

where μ_0 is the permeability of free space, NI is the number of amp-turns exciting each pole tip, and f is the circular bore radius. The ideal pole tip shape is determined from conformal mapping [17] assuming infinitely long poles so that for any finite size device, the quadrupole field will be contaminated with higher order multipoles. Rectangular aperture quadrupoles, often known as Panofsky quadrupoles (PQs) [18], are composed of current sheets surrounded by a soft iron yoke and do not suffer from such machining limitations. The cross section of a PQ is shown in Fig. 2(a). Draper *et al.* [19] showed theoretically that this geometry creates a pure dipole or quadrupole field (i.e., no higher order multipoles), depending on coil excitation, across the *entire* bore region. There are two major drawbacks of the PQ compared to conventional quadrupoles. First, as a current-dominated magnet that also has magnetic material, the field quality is very sensitive to conductor location [20]. This drawback is somewhat mitigated by the high alignment accuracy of microfabrication methods. The other drawback is the magnetic field gradient is ∼4× lower than a conventional quadrupole with the same bore size and NI. As such, PQs are typically only used where wide apertures are required, such as in spectrometers [18,21], beam injection [22], and beam extraction [23]. More novel interpretations such as the twin-aperture PQ [24] and tunable combined function PQ [25–27] show the versatility of this magnet type. The highest gradient of any of these PQs was 15 T/m.

Despite the apparent drawbacks associated with using PQs, there are a few very important advantages to using MPQs as compact quadrupole magnets. First, the gradient scales favorably as the gap decreases as $1/g$. Second, while the microfabrication of conventional quadrupole magnets [14] is very difficult and suffers from low yield and reliability, the fabrication of the MPQ is very simple by comparison, and the resulting device is more robust. Third, the magnetic length of the microscale conventional quadrupole is limited to ∼1 mm, but the magnetic length of the MPQ is limited only by substrate size (typically greater than 100 mm). Therefore, the inherently lower gradient of the MPQ can be compensated by a longer length.
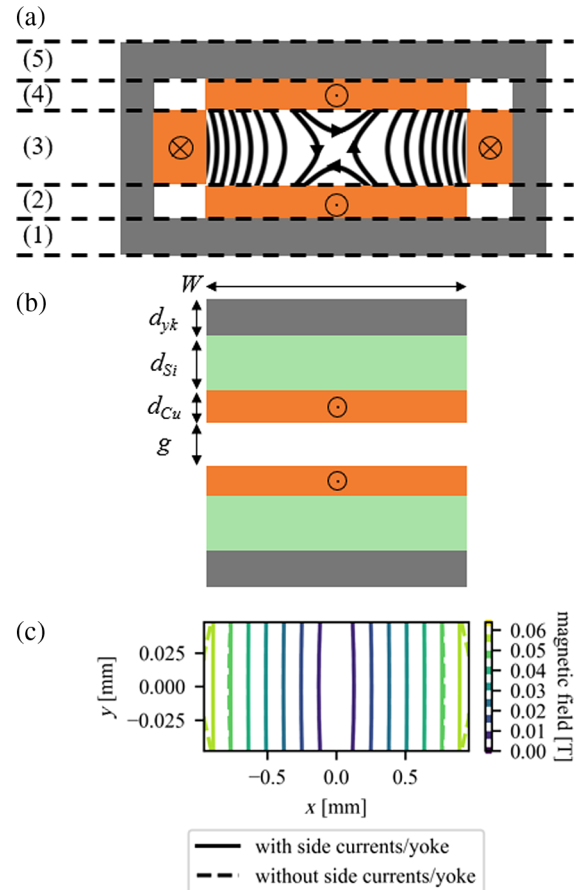

FIG. 2. (a) Depiction of PQ and its magnetic field contours. The current sheets are orange and are surrounded by the gray magnetic yoke. The microfabrication layers are delineated with dashed lines. (b) The cross section of the MPQ, showing the device geometry parameters (L is not shown but is simply the extrusion length of the cross section into the page). Orange is copper, green is silicon, and gray is the magnetic yoke. (c) The magnitude of the transverse magnetic field of a relatively wide PQ ($W = 2$ mm and $g = 0.1$ mm) with side currents and yokes (solid lines) and without (dashed lines). All appreciable variation is at the edges of the bore region.

The PQ can be visualized in a series of layers as shown in Fig. 2(a), which makes it amenable to microfabrication processes. A possible processing flow could be to form the (1) bottom magnetic yoke, (2) bottom thin copper trace, (3) side traces and yoke, (4) top thin copper trace, and (5) top magnetic yoke. The third layer thickness, which could exceed 100 μm, is potentially problematic because electroplated film thicknesses greater than a few hundred microns often suffer from stress-induced delamination. One could consider a hybrid device where most of the MPQ is microfabricated and the third layer is conventionally machined, but such approaches would have many issues to address in how to align, mount, and electrically insulate the various individual parts. The solution explored in this work is simpler: design the device width to be much larger than

TABLE I. Simulated device parameters.

J (A/m^2)	Current density	1×10^8
d_{Cu} (μm)	Copper thickness	50
d_{yk} (μm)	Yoke thickness	50
d_{Si} (mm)	Distance between copper and yoke	0.6
W (mm)	Device width	2
g (mm)	Gap between MPQ halves	Variable
L (mm)	Device length	6.7

other dimensions. In this way, the side traces and yoke can be omitted, as shown in Fig. 2(b), because they contribute little to the field in the magnet center. We confirmed this hypothesis, shown in Fig. 2(c), using a COMSOL Multiphysics simulation of the magnetic field magnitude of a device with parameters shown in Table I. Note the extreme aspect ratio in the figure. We also see the magnetic field magnitude of the devices with and without side currents and yokes differ only near the device edges. A consequence of this result is that the top and bottom halves can be fabricated separately (possibly on the same silicon substrate), then assembled in the correct configuration with a mounting fixture.

II. THEORY

Hand and Panofsky derived an expression to predict the gradient of the original rectangular aperture quadrupole using the standard assumptions that the device is very long and the permeability of soft magnetic material is very high. For the MPQ, we impose the additional condition that the width is large compared to other dimensions. With these conditions, the MPQ gradient, B', can be derived to be

$$B' = \frac{\mu_0 J}{1 + \frac{g}{2d_{Cu}} + \frac{d_{Si}}{d_{Cu}}} = \frac{\mu_0 I}{W} \frac{1}{d_{Cu} + \frac{g}{2} + \frac{d_{Si}}{2}}, \quad (1)$$

where the total current is $I = J \times d_{Cu} \times W$. Other parameters are explained in Table I. This expression is equivalent to that derived by Hand and Panofsky if $d_{Si} = 0$, as was the case for the original Panofsky quadrupole. We show in the Appendix that the calculated gradient of Eq. (1) matches that of finite element simulations as long as the geometry satisfies all the previously mentioned assumptions.

We need to assess how wide the MPQ needs to be to generate a good quality quadrupole field. The PQ has a pure quadrupole field, so this is also the goal for the MPQ. We show the normalized absolute values of the normal multipoles as a function of width in Fig. 3 for the geometry shown in Fig. 2(b) as calculated in COMSOL Multiphysics. We used the convention where $n = 1$ is the dipole moment, $n = 2$ is the quadrupole moment, $n = 3$ is the sextupole moment, and so on. The simulated device possessed the nominal device parameters from Table I except with a gap of 1.5 mm to compare with experimental results.
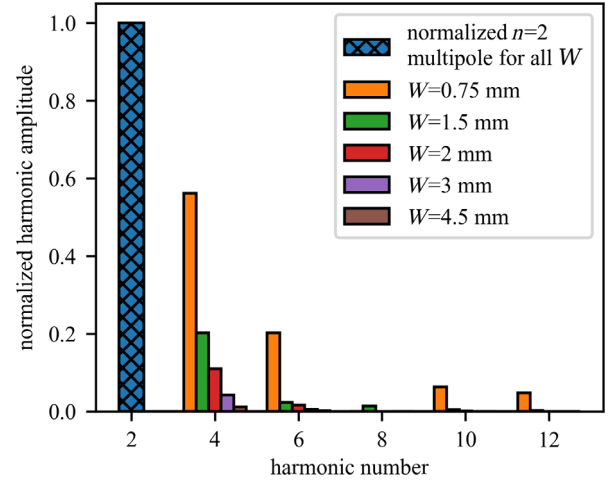

FIG. 3. A 2D harmonic analysis of the device as a function of width was computed using COMSOL Multiphysics. All multipoles are normalized to the $n = 2$ quadrupole moment (blue hatched bar). The gap was set to 1.5 mm.

The distribution of higher order multipoles depends on all the geometry parameters, not just the width, but in all cases, the higher order multipoles are suppressed as the width increased. For example, as shown in the figure, if $d_{Si} = 0.6$ mm, the width/gap ratio W/g needs to be approximately 3 to suppress the next largest harmonic, $n = 4$, to less than 1%. Not shown in the figure, however, is that if $d_{Si} = 0$ then only $W/g = 2.5$ is required to achieve the same level of harmonic suppression. All skew moments are zero and are therefore not shown.

III. THREE-DIMENSIONAL MAGNETIC SIMULATIONS WITH LEADS

The MPQ has symmetric electrical leads to facilitate current flow into the quadrupole active region. In this section, we present RADIA [28] simulations to provide a more complete view of device behavior including the device and PCB leads. The device parameters for this section are the same as for the previous section simulations, with the gap set to 1.5 mm to better compare with experimental results shown in the next section.

Figure 4 shows the integrated magnetic field harmonic components. The quadrupole moment ($n = 2$) has a value of 0.0153 T. The effective length is computed to be 4.1 mm (computed by integrating the gradient profile and dividing by the maximum gradient), despite the active region measuring physically to be 6.7 mm long. This is due in part to the curved nature of the leads. The current is directed completely in the z direction only over about 1 mm; the current in the rest of the device also has some x component due to the curved nature of the leads, which in effect reduces the amount of current traveling in the z direction. We see nonzero multipoles at every even order and a nonzero skew dipole moment ($n = 1$), indicating the
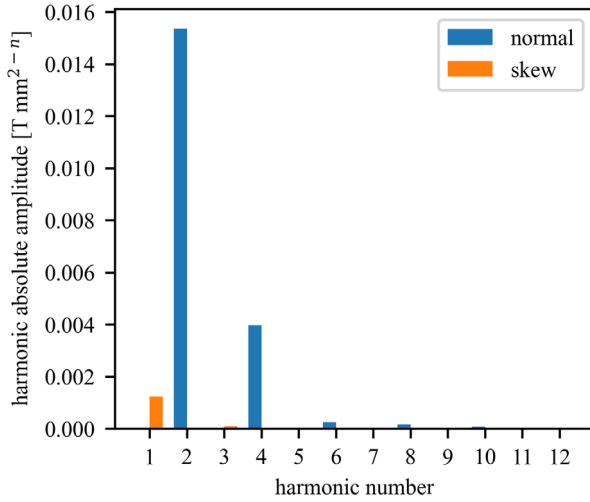
FIG. 4.   3D harmonic analysis of device and PCB together using nominal parameters and a gap of 1.5 mm.

presence of a dipole magnetic field in the x direction. We can attribute the skew dipole moment to the leads of the device and PCB because it is present in the 3D simulations that include the leads but not in the 2D simulations of Fig. 3.
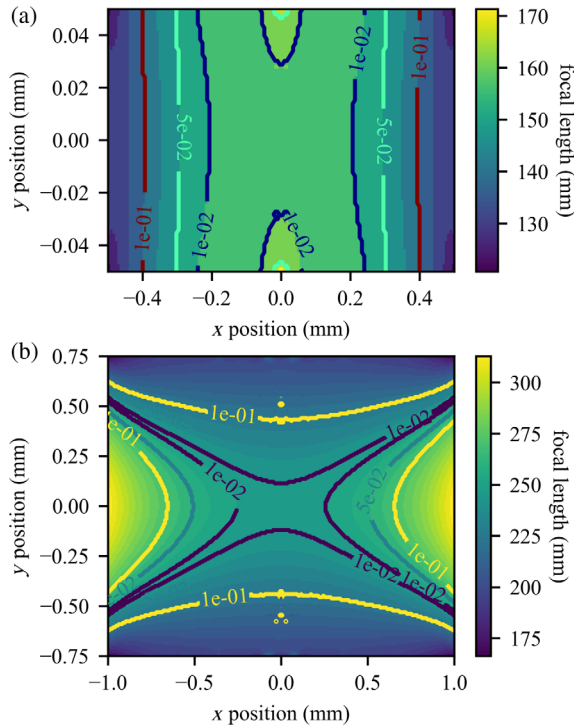

FIG. 5.   Device focal length in millimeters at a beam energy of 3.2 MeV, showing aberrations in device with a current of 20 A ($J = 2 \times 10^8$ A/m^2) for the (a) small aperture (1 mm width, 0.1 mm gap) devices and (b) large aperture (2 mm wide, 1.5 mm gap) devices. The colormap shows the focal length across the device aperture, and the contour lines show the 1%, 5%, and 10% "good focal length" regions.

We simulated two devices using RADIA and used focal length variation as a measurement of field quality. A tiny pencil beam was propagated through the devices with various initial transverse offsets across the entire bore region, and the z position of the beam waist was determined to be the focal length. The beam energy was chosen to be 3.2 MeV to correlate with the experimental work in the next section. The results are shown in Fig. 5. The first device has a small aperture (1 mm wide and 0.1 mm gap) and the second device has a larger aperture corresponding to the experimental device (2 mm wide and 1.5 mm gap). For the small aperture, the focal length variation is $+10\%/-23\%$; these values represent the maximum and minimum values of focal length anywhere within the magnet aperture, expressed as fractional errors relative to the on-axis focal length. The 1% good field region size is 0.33×0.06 mm^2. For the large aperture device, the focal length variation is $+27\%/-33\%$, and the size of the 1% good field region is 0.5×0.25 mm^2. As expected, the field quality and relative size of the good field region are much better in the small aperture device than in the large aperture device. This is mostly due to the larger W/g ratio.

IV. EXPERIMENTAL WORK

A. Fabrication

The fabrication process flow for this device is shown in Fig. 6(a). First, the silicon is electrically insulated by depositing 300-nm silicon nitride on both sides of the 0.6-mm thick wafer using low-pressure chemical vapor deposition (Tystar Titan II). We sputter an electroplating seed layer of 40 nm titanium and 300 nm copper (CVC 601) on the wafer backside. We use a thick film photoresist (AZ 50XT) to define the yoke region and electroplate the permalloy yoke to a height of 50 μm [29]. We then sputter an electroplating seed layer on the front side, use a thick film photoresist to define the copper trace region, then electroplate copper (Technic Elevate Cu 6320) to a height of 50 μm. The wafer is diced using a wafer saw, and the devices are mounted on a PCB for testing as shown in Fig. 6(b). Electrical interface from device to PCB is achieved with soldered thick copper sheets to handle 10s of Amperes of current [Fig. 6(b)]. The PCB-mounted devices are aligned on their respective aluminum mount pieces, then brought together as shown in Fig. 6(c).

B. Thermal characterization

Thermal simulations were performed using COMSOL™ for three potential devices and compared with experimental measurements obtained from a thermal camera (ThermalExpert TE-Q1 Pro) using the right PCB-mounted device from Fig. 6(b), and the results are shown in Fig. 7. The first modeled device (curve 1 in the figure) is that of the MPQ fabricated in PCB material, i.e., with copper traces embedded directly into PCB material. The second device (curve 2) is a
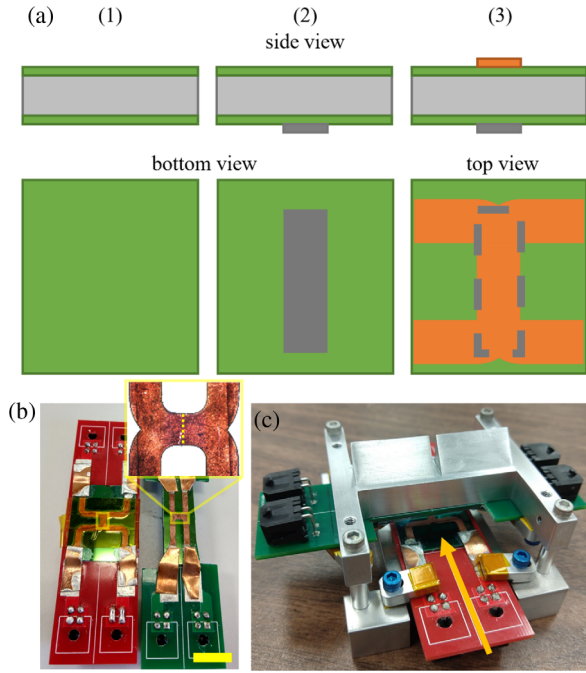
FIG. 6. (a) Fabrication flow showing the side and top/bottom views of fabrication steps of (1) electrical insulation of silicon wafer (gray) using silicon nitride (green), (2) yoke electroplating (dark gray), and (3) copper electroplating (orange) on the opposite side, with the yoke extents shown by dashed lines. (b) MPQs mounted on PCBs. The yellow scale bar is 1 cm. The region of the quadrupole is shown by a yellow box for each half of the MPQ, and the inset is an optical microscope image of the right device's active region. The dotted yellow line across the device has a length of 2 mm. (c) the fully assembled MPQ in the aluminum mount, with the beam propagation direction shown by the orange.
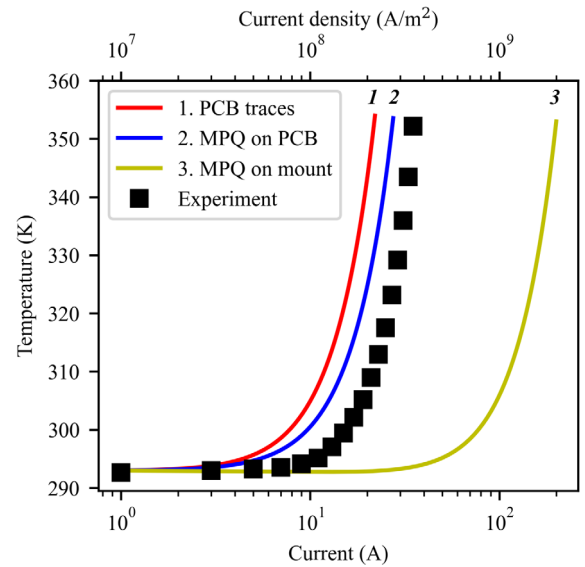

FIG. 7. Steady-state COMSOL thermal simulations at room temperature of devices fabricated in (1) PCB (FR4) material, (2) silicon mounted on PCB, and (3) silicon mounted on a cooled metal mount, compared with the experimental device (similar to device 2). The top x axis is simply a scaled version of the bottom x axis.

MPQ fabricated on silicon and mounted on a PCB as demonstrated in this work. In both cases, the model assumes the PCB is mounted on a thermal reservoir held at 293 K. One example of a constant temperature thermal reservoir could be an actively cooled metal block. The third device (curve 3) is a MPQ fabricated in silicon and mounted directly to the thermal reservoir. The maximum steady-state temperature of the devices as a function of current is plotted in Fig. 7. We see that the all-PCB device can tolerate the least amount of current per unit temperature change, followed closely by the MPQ mounted on a PCB. The PCB-fabricated device performs poorly because of the typically small [$\sim$1 W/(mK)] thermal conductivity of PCB material at room temperature. The silicon-fabricated, PCB-mounted device performs slightly better as the silicon has much higher thermal conductivity [$\sim$100 W/(mK)] and spreads the generated heat over a wider area but still suffers from high PCB thermal resistance. The MPQ mounted directly on a metallic mount can tolerate approximately 10 times more current than the PCB-mounted MPQ because there is no thermally resistive PCB material. We see that the fabricated device tolerates more current than

the corresponding simulated PCB-mounted silicon-fabricated device, which we attribute to the large copper electrical leads soldered to the device. These leads can dissipate substantial heat but were not included in the COMSOL model. Another small source of error in this experiment (which was not conducted in vacuum) could be air convection, which also was not included in the COMSOL model, but this is unlikely because the thermal conductivity of air [$\sim$0.025 W/(mK)] is much smaller than that of PCB material.

Using pulsed instead of dc current would permit higher current densities without as much heating. The inductance and resistance of a yokeless device are approximately 50 nH [30] and 3 mΩ respectively, resulting in an RL time constant of approximately 16 μs. Using a standard time of three time constants corresponds to a frequency of 20 kHz. This is an upper bound on the operating frequency, as the inclusion of the yoke will increase the inductance and therefore decrease the operating frequency.

C. Direct field measurement via Hall probe

We first used a Hall probe to map the magnetic field in the MPQ. The gap was set to 5.6 mm to accommodate the Hall probe thickness, and the total current through each MPQ half was 20 A (2×10^8 A/m^2). We measured $B' = dB_y/dx$, the transverse gradient, along the z axis, which is the beam propagation direction. The experimental results match magnetostatic simulations from RADIA within 10% which is shown in Fig. 8. There is no flattop region, which means that fringe effects dominate the gradient profile. This is to be expected, because the gap is similar
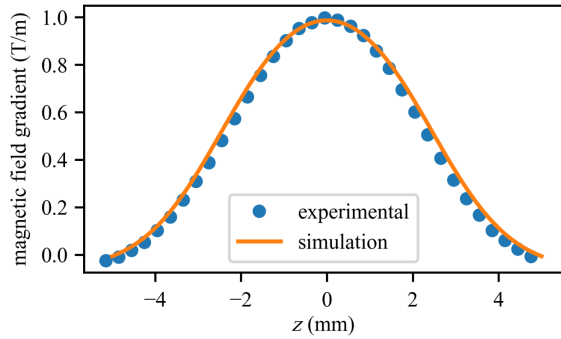
FIG. 8. Measured gradient (dB_y/dx) along z axis at $x = y = 0$ at a current of 20 A (2×10^8 A/m^2) and a 5.6-mm gap.

to the physical length of the quadrupole. It has been suggested by Wiedemann [31] that a more correct calculation for the effective length in situations with pronounced fringe effects can be done by "slicing" the magnet into a

series of thin hard-edged magnets and using a matrix multiplication based approach [32]. Using this methodology yields an effective length (at the nominal beam energy of 3.2 MeV) of 5.4 mm. For reference, the conventional definition of effective length as the integral of the gradient profile divided by the maximum gradient yields an effective length of 4.8 mm.

D. Electron beam measurement

Focusing of a relativistic electron beam was performed at the UCLA Pegasus beamline [33]. The electron beam from the radiofrequency photoinjector [34] is accelerated to an energy of 3.2 MeV ($\gamma = 7.24$), focused by the MPQ, then imaged on a screen 0.5 m downstream by a Princeton Instruments PI-MAX 3 camera. The solenoid at the electron gun exit is used to collimate the beam, and no other focusing magnets were used. The MPQ gap was set to
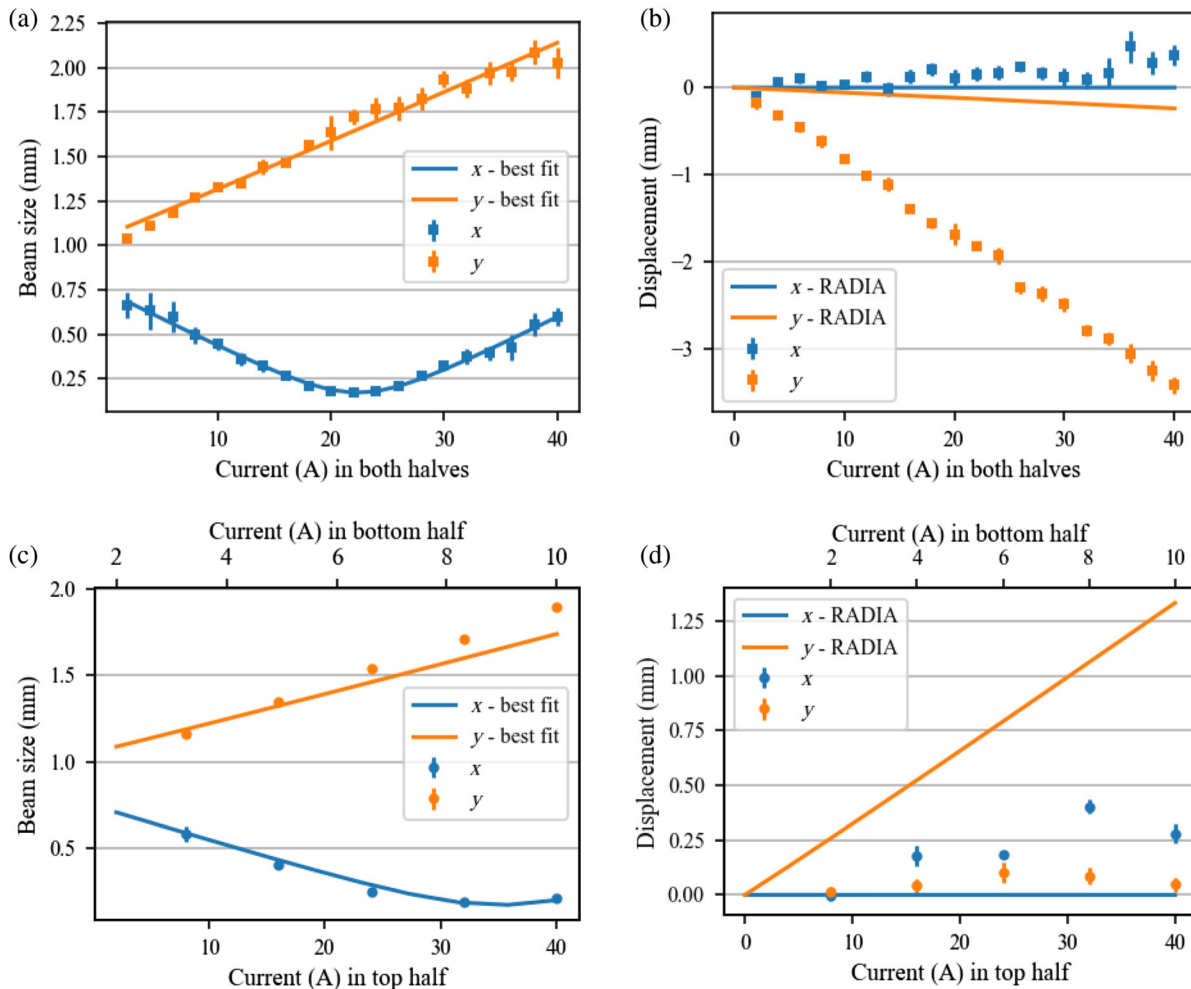

FIG. 9. Beam size and beam displacement as a function of the current magnitude. (a) and (b) Beam size and displacement, respectively, where the current in both halves was the same. (c) and (d) Compensated experiment, where the top half used 4 times as much current as the bottom half to cancel the beam displacement in the y direction. The error bars, many too small to see, denote 1 standard deviation of at least five measurements. The solid lines in (a) and (c) are parabolic least squares fits, and the solid lines in (b) and (d) are RADIA simulations to show the simulated displacement.

1.5 mm for these experiments. At least five images were taken for each current value, both before and while the MPQ was powered. For each shot, the beam intensity distribution recorded on the screen was fit using a two-dimensional Gaussian model. The average rms beam spot sizes in the x and y directions for the different quadrupole currents are plotted in Figs. 9(a) and 9(c), and the errors in the measurements correspond to the standard deviation in the data. The beam displacements displayed in Figs. 9(b) and 9(d) in x and y is calculated as the beam centroid shift between shots with the MPQ powered and not powered.

For the first experiment [Figs. 9(a) and (b)], the current in both MPQ halves was equal and in the $-z$ direction (for clarity, the current magnitude is plotted). As shown in Fig. 9(a), the beam was focused to a waist in the x direction at a current of 22 A to 168 μm. The y beam size continually increases as a function of the driving current as expected. The solid lines show the least-squares parabolic fit [35] from which we can extract the input beam distribution second-order moments: $\sigma_{x0} = 1.12$ mm, $\sigma_{xx'} = 8.9 \times 10^{-7}$ m, $\sigma_{x'0} = 8.6 \times 10^{-4}$, $\sigma_{y0} = 0.98$ mm, $\sigma_{yy'} = 4.3 \times 10^{-8}$ m, $\sigma_{y'0} = 8.6 \times 10^{-4}$.

While the RADIA simulation predicted a small vertical displacement [as seen by the solid orange line in Fig. 9(b)], essentially due to the skew dipole moment calculated in Fig. 4, the measured displacement was much larger. We found experimentally that the displacement could be compensated by using approximately 4 times more current in the top MPQ half. This effectively superimposes an additional B_x dipole component over the quadrupole field which counteracts other sources of vertical deflection. We show the beam size and displacement in this compensated scenario in Figs. 9(c) and 9(d). Without compensation, the vertical beam displacement was over 3 mm at 40 A [Fig. 9(b)] but with current compensation, the vertical displacement was reduced to less than 0.15 mm [Fig. 9(d)]. Due to the 40-A limitation of the power supply, we could only approach the desired focal length for the compensated case in Fig. 9(c), but we see that the beam envelopes using the fit parameters from the previous paragraph still matches the experimental data within the error bars.

In order to find the source of the deflection, we first ruled out any major fabrication errors by measuring each MPQ half separately with the Hall probe; the measured fields largely matched RADIA simulations. We then realized that some electrical connection wires to the bottom half of the MPQ, approximately 100 mm long, may not have been routed away sufficiently from the beam axis during the experiment. We show in Fig. 10 the effect such wires could have on the beam, in both x (horizontal) and y (vertical) directions. We note here that these leads do not appreciably affect the quadrupole focal length. For this particular simulation case, the total displacement is 1 mm at 22 A, whereas the experimentally measured displacement was nearly 2 mm. However, we do not know the exact location
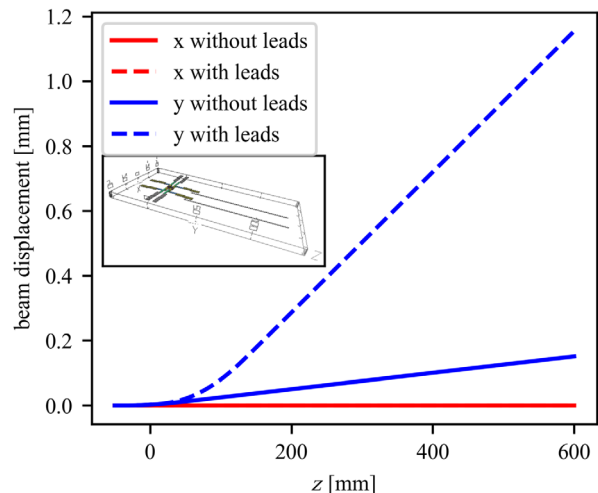

FIG. 10. RADIA simulations without (solid lines) and with (dashed lines) extra 100-mm long leads on the back of the device, showing the effects on the overall beam displacement in both x and y directions.

or angle of these wires during the experiment which prevents a full quantitative comparison with the data. Nevertheless, the extra wires are likely responsible for the vertical deflection observed in the experiment.

V. OUTLOOK AND CONCLUSIONS

There are several other ways in which a second-generation MPQ could improve substantially on the proof-of-concept shown here.

Using through-silicon vias would improve the field quality significantly. Such vias route the current to the backside of the substrate instead of to the sides, which mostly eliminates harmful fringing entrance fields. Ensuring conductor and yoke flatness by using chemical-mechanical polishing would also aid in reducing field errors.

The gradient can be increased substantially by using smaller gaps (and more focused electron beams) and also using higher current densities than demonstrated in this work. We show RADIA simulations in Fig. 11 of the gradient in the center of the device as a function of gap and current density, where we see that gradients could reach 100 s T/m for a small gap, thermally optimized (because of the high currents) device. We used a yoke thickness of 300 μm for these simulations to avoid yoke saturation, but saturation effects can still be seen in this figure. We can see at $g = 10^{-2}$ mm, from $J = 6 \times 10^8$ A/m² to $J = 1 \times 10^9$ A/m², the center gradient *decreases* as the current density *increases*. This occurs because the yoke saturates, causing the gradient in the device center to decrease somewhat while the gradient near the device edges increases substantially. While the center gradient recovers with increasing current, the gradient uniformity cannot be recovered after the onset of saturation. Designs with thicker yokes like the one simulated and shown here are therefore favored for future generations of the MPQ.
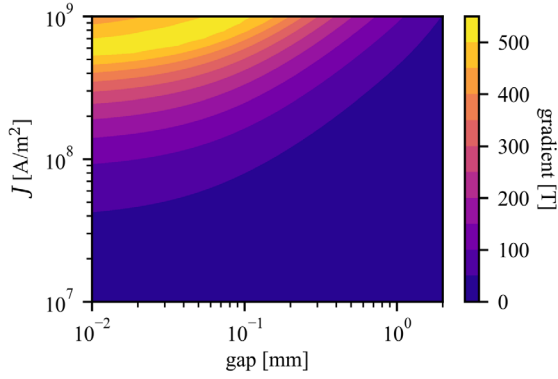
FIG. 11.   RADIA simulations showing the maximum gradient of the MPQ with $d_{Si} = 5$ μm and $d_{yk} = 300$ μm.

As a concrete example of how reducing d_{Si} improves the efficiency and utility of the MPQ, consider a fairly typical small bore (8 mm) quadrupole magnet used in the undulator section of the Linac Coherent Light Source [36] that has a maximum integrated gradient of 3.6 T and consumes 27 W in the magnet coils. This equates to 0.13 T/W or 0.13 T of integrated gradient per watt of power. The total power consumption of both halves of the MPQ, not including extraneous wiring, was measured to be approximately 0.34 W at 10 A. With nominal parameters in Table I, we calculate the integrated gradient via RADIA simulation to be 0.043 T, and so the integrated gradient per watt of power expended is also calculated to be 0.13 T/W for the MPQ. That is with large d_{Si}, however; with $d_{Si} = 0$ the integrated gradient is 0.27 T at 10 A. The power loss would be the same (0.34 W), which leads to 0.79 T/W, which is approximately 6 times higher than the conventional quadrupole.

In conclusion, we presented the design, fabrication, and characterization of a microfabricated Panofsky-style quadrupole. We successfully demonstrated the focusing of a 3.2-MeV electron beam. We also observed a large vertical displacement which is attributed to electrical leads. We presented several improvements in a next-generation device to reduce the various deleterious effect of the electrical leads and boost the gradient.

ACKNOWLEDGMENTS

APPENDIX: COMSOL CONFIRMATION OF ANALYTICAL GRADIENT FORMULA

We investigated the limits over which Eq. (1) is valid using COMSOL. The simulations were 2D, as is the magnetic circuit analysis used to derive Eq. (1). The nominal parameters for the analysis are shown in Table I. We used

several different yokes. The "ideal" yoke has a fixed, high relative permeability of 8500 (corresponding to the measured low field permeability of the electroplated permalloy [29]). Magnetic saturation is not included in a constant permeability model and so the yoke thickness makes little difference—this was verified in simulations not shown here. We also simulated yokes with the measured MH curve of the electroplated permalloy with thicknesses of 50 and 300 μm to show saturation effects. We include a "yokeless" MPQ, which is represented by two rectangular prisms of dimensions W, d_{Cu}, L, in the x, y, and z dimensions, respectively, separated by a gap g, with the current directed in the z direction. The 3D yokeless gradient in the center of the device can be derived to be

$$B'_{3D} = \frac{2\mu_0 J}{\pi} \left[\arctan\left(\frac{L}{W} \frac{g + 2d_{Cu}}{\sqrt{W^2 + (d_{Cu} + g)^2 + L^2}} \right) \right.$$
$$\left. - \arctan\left(\frac{L}{W} \frac{g}{\sqrt{W^2 + (d_{Cu} - g)^2 + L^2}} \right) \right] \quad \text{(A1)}$$

which by letting $L \to \infty$ yields the two-dimensional expression for the yokeless gradient:

$$B'_{2D} = \frac{2\mu_0 J}{\pi} \left[\arctan\left(\frac{2d_{Cu} + g}{W} \right) - \arctan\left(\frac{g}{W} \right) \right] \quad \text{(A2)}$$

We first investigated the relationship of gradient and device width in the case of constant current density, shown in Fig. 12. As Eq. (1) does not depend on W in the case of constant current density, we expect the relationship of B' and W to be constant, but FEM simulations in Fig. 12(a) show very different behavior. We see for large widths, the gradient matches Eq. (1) except for where the thin yoke saturates (around $W = 5$ mm). At very small device widths, where the "large width" assumption is invalid, the behavior resembles that of the yokeless MPQ. The transition point between these two behaviors is around $W = 1$ mm for this geometry. The "critical width" at which the maximum gradient occurs for two copper sheets can be derived to be $W_c = \sqrt{g(g + 2d_{Cu})}$. For $g = 0.1$ mm and $d_{Cu} = 50$ μm, we calculate $W_c = 0.14$ mm, which matches Fig. 12(a). At even smaller widths, however, the largeness of the gap compared to the device width affects performance and the gradient approaches zero.

In addition to the gradient's dependence on device width, we also investigated in Fig. 12 the effects of varying the gap (part b), silicon thickness (part c), and copper thickness (part d). We see good agreement in general; the few instances of poor agreement stem from breaking the derivation assumptions that lead to Eq. (1). For example, we see that all FEM results depart from the analytical expectation in Fig. 12(a) for small widths compared to other dimensions. Magnetic saturation, which would violate the derivation assumptions, is evident in the simulation
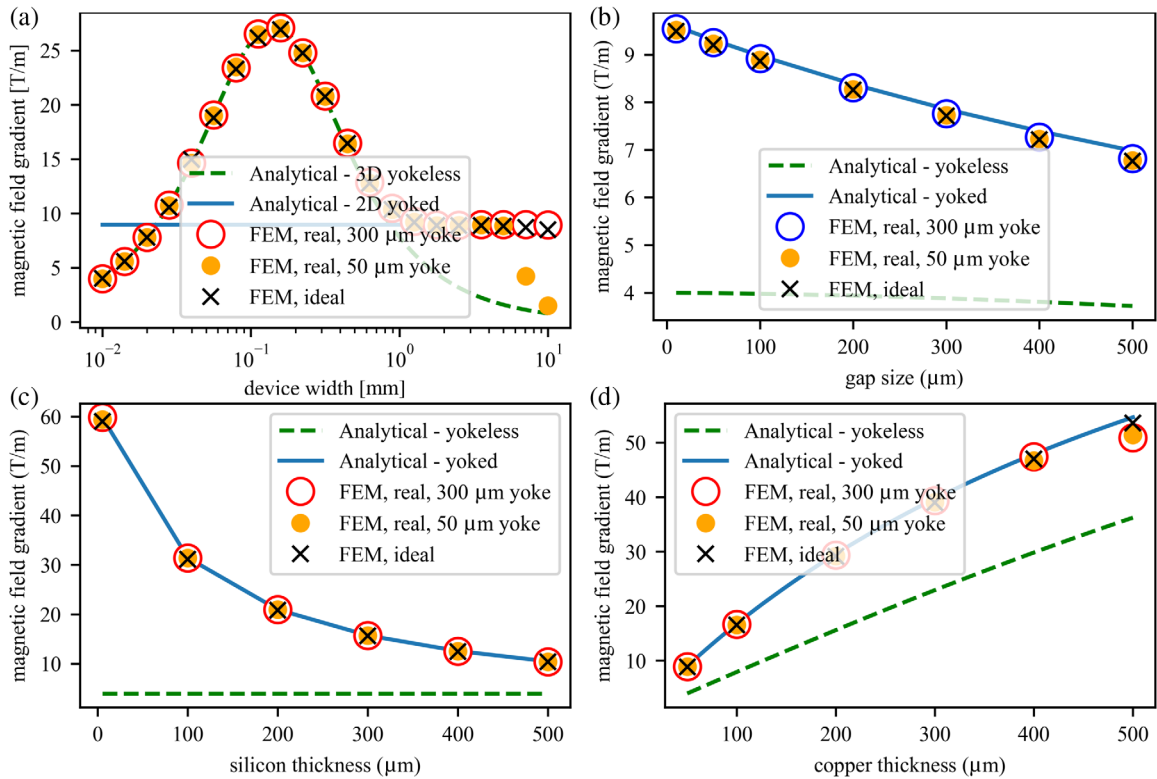
FIG. 12. Comparison of theory and simulation for the center MPQ magnetic field while changing the (a) width W, (b) gap g, (c) silicon thickness d_{Si}, and (d) copper thickness d_{Cu}. The ideal material is assumed to have a fixed relative permeability of 8500 (i.e., no saturation), whereas the real material utilizes experimentally measured MH curves. The gradient is the value of dB_y/dx, measured at the center of the device.

when (i) the ideal material model (fixed permeability) behavior differs from that of the models that incorporate "real" magnetic material properties or (ii) when the behaviors of the models with thin and thick yoke material are different. We can see the effects of magnetic saturation in Fig. 12(d) at large copper thicknesses. The ideal yoke model tracks perfectly with the analytical 2D result, but the results incorporating the actual magnetic properties differ at large copper thicknesses which is an indication of magnetic saturation in the yoke.

[1] J. B. Rosenzweig *et al.*, An ultra-compact x-ray free-electron laser, New J. Phys. **22,** 093067 (2020).

[2] M. E. Couprie, Towards compact free electron–laser based on laser plasma accelerators, Nucl. Instrum. Methods Phys. Res., Sect. A **909,** 5 (2018).

[3] S. V. Kutsaev, Novel technologies for compact electron linear accelerators (review), Instrum. Exp. Tech. **64,** 641 (2021).

[4] M. K. Weikum *et al.*, Eupraxia—a compact, cost-efficient particle and radiation source, AIP Conf. Proc. **2160,** 040012 (2019).

[5] E. Sicking and R. Ström, From precision physics to the energy frontier with the compact linear collider, Nat. Phys. **16,** 386 (2020).

[6] A. Nevelsky, Z. Bernstein, R. Bar-Deroma, A. Kuten, and I. Orion, Design and dosimetry characteristics of a commercial applicator system for intra-operative electron beam therapy utilizing ELEKTA Precise accelerator, J. Appl. Clin. Med. Phys. **11,** 57 (2010).

[7] S. Kutsaev, R. Agustsson, A. Arodzero, S. Boucher, J. Hartzell, A. Murokh, F. O'Shea, and A. Y. Smirnov, Electron accelerators for novel cargo inspection methods, Phys. Procedia, **90,** 115 (2017).

[8] Y. Chen, Nanofabrication by electron beam lithography and its applications: A review, Microelectron. Eng. **135,** 57 (2015).

[9] D. Abliz, Y. Duan, L. Steuernagel, L. Xie, D. Li, and G. Ziegmann, Curing methods for advanced polymer composites—a review, Polym. Polym. Compos. **21,** 341 (2013).

[10] H. Zahedmanesh, O. V. Pedreira, C. Wilson, Z. Tőkei, and K. Croes, Copper electromigration; Prediction of scaling limits, in *Proceedings of IEEE International Interconnect Technology Conference, IITC-2019, Brussels, Belgium* (IEEE, New York, 2019).

[11] C. Lee, Z. Wu, Y. Xuan, R. J. England, and M. Qi, Novel fabrication of 3D woodpile accelerator by silicon membrane stacking, AIP Conf. Proc. **1777,** 060005 (2016).

[12] K. Cheung, L. Velásquez-García, and A. Akinwande, Fully batch-fabricated linear quadrupole mass filters, in *Proceedings of 2008 Solid-State, Actuators, and Microsystems Workshop Technical Digest* (Transducer Research Foundation, Hilton Head, SC, 2008), pp. 316–319.

[13] D. S. Black, K. J. Leedle, Y. Miao, U. Niedermayer, R. L. Byer, and O. Solgaard, Laser-Driven Electron Lensing in Silicon Microstructures, Phys. Rev. Lett. **122,** 104801 (2019).

[14] J. Harrison, Y. Hwang, O. Paydar, J. Wu, E. Threlkeld, J. Rosenzweig, P. Musumeci, and R. Candler, High-gradient microelectromechanical system quadrupole electromagnets for particle beam focusing and steering, Phys. Rev. ST Accel. Beams **18,** 023501 (2015).

[15] T. Godlove, S. Bernal, and M. Reiser, Printed-circuit quadrupole design, in *Proceedings of the Particle Accelerator Conference, Dallas, TX, 1995* (IEEE, New York, 1995), Vol. 4, pp. 2117–2119.

[16] W. W. Zhang, S. Bernal, H. Li, T. Godlove, R. A. Kishek, P. G. O'Shea, M. Reiser, V. Yun, and M. Venturini, Design and field measurements of printed-circuit quadrupoles and dipoles, Phys. Rev. ST Accel. Beams **3,** 122401 (2000).

[17] K. Halbach, Understanding modern magnets through conformal mapping, Int. J. Mod. Phys. B **04,** 1201 (1990).

[18] L. N. Hand and W. K. H. Panofsky, Magnetic quadrupole with rectangular aperture, Rev. Sci. Instrum. **30,** 927 (1959).

[19] J. E. Draper, Beam steering with quadrupole and with rectangular box magnets, Rev. Sci. Instrum. **37,** 1390 (1966).

[20] R. Auzolle, F. Kircher, and J. P. Penicaud, A Panofsky-type superconducting quadrupole with a very high gradient homogeneity, IEEE Trans. Nucl. Sci. **28,** 3228 (1981).

[21] R. Peterson, J. Kraushaar, R. Ristinen, H. Thiessen, and M. Rickey, A versatile multipole correction magnet of rectangular aperture, Nucl. Instrum. Methods **129,** 47 (1975).

[22] Y. Li, P. Chin, R. Kishek, M. Reiser, M. Venturini, J. Wang, Y. Zou, and T. Godlove, Design, simulation and test of pulsed Panofsky quadrupoles, in *Proceedings of the 18th Particle Accelerator Conference, New York, 1999* (IEEE, New York, 1999), pp. 3369–3371.

[23] S. Masubuchi and T. Nakanishi, Panofsky magnet for the beam extraction from the synchrotron using a fast q-magnet and rf-knockout, Nucl. Instrum. Methods Phys. Res., Sect. B **269,** 2911 (2011).

[24] M. Sullivan, K. Bertsche, P. Vobly, E. Paoloni, S. Bettoni, and P. Raimondi, A new interaction region design for the Super-B Factory, in *Proceedings of the International Particle Accelerator Conference, IPAC-2010, Kyoto, Japan* (ICR, Kyoto, 2010), Vol. 7, p. 4.

[25] K. Melconian, C. Collins, K. Damborsky, J. Kellams, P. McIntyre, N. Pogue, and A. Sattarov, Design of a MgB_2 beam transport channel for a strong-focusing cyclotron, IEEE Trans. Appl. Supercond. **24,** 1 (2014).

[26] G. H. Biallas, N. Belcher, D. Douglas, T. Hiatt, and K. Jordan, Combined Panofsky quadrupole corrector dipole, in *Proceedings of the 22nd Particle Accelerator Conference, PAC-2007, Albuquerque, NM* (IEEE, New York, 2007), pp. 602–604.

[27] J. Budnick, T. Hall, D. Li, and S. Y. Lee, Design, fabrication and experimental results of a multi-purpose Panofsky magnet, Nucl. Instrum. Methods Phys. Res., Sect. A **368,** 572 (1996).

[28] O. Chubar, P. Elleaume, and J. Chavanne, A three-dimensional magnetostatics computer code for insertion devices, J. Synchrotron Radiat. **5,** 481 (1998).

[29] M. Glickman, T. Niblock, J. Harrison, I. Goldberg, P. Tseng, and J. Judy, High permeability permalloy for MEMS, in *Proceedings of 2010 Solid-State, Actuators, and Microsystems Workshop Technical Digest* (Transducer Research Foundation, Hilton Head, SC, 2010), pp. 328–331.

[30] F. E. Terman, *Radio Engineers' Handbook* (McGraw-Hill, New York, 1943).

[31] H. Wiedemann, *Particle Accelerator Physics* (Springer International Publishing, New York, 2015).

[32] H. Jia and M. Plum, Fringe field overlap model for quadrupoles, in *Proceedings of the 13th Symposium on Accelerator Physics, SAP2017, Jishou, China* (JACoW, Geneva, Switzerland, 2018).

[33] K. Kabra, S. Li, F. Cropp, T. J. Lane, P. Musumeci, and D. Ratner, Mapping photocathode quantum efficiency with ghost imaging, Phys. Rev. Accel. Beams **23,** 022803 (2020).

[34] D. Alesini, A. Battisti, M. Ferrario, L. Foggetta, V. Lollo, L. Ficcadenti, V. Pettinacci, S. Custodio, E. Pirez, P. Musumeci, and L. Palumbo, New technology based on clamping for high gradient radio frequency photogun, Phys. Rev. ST Accel. Beams **18,** 092001 (2015).

[35] E. Prat, Symmetric single-quadrupole-magnet scan method to measure the 2D transverse beam parameters, Nucl. Instrum. Methods Phys. Res., Sect. A **743,** 103 (2014).

[36] P. Emma, E. Bong, H.-D. Nuhn, C. Rago, C. Spencer, and J. Welch, Electro-magnetic quadrupole magnets in the ICLS FEL undulator, SLAC National Accelerator Laboratory, Menlo Park, CA, Technical Report No. SLAC-TN-05-016, 2005, 10.2172/839676.